REPORT DOCUMENTATION PAGE

Form Approved OMB No. 0704-0188

1. REPORT DATE *(DD-MM-YYYY)*	2. REPORT TYPE	3. DATES COVERED *(From - To)*
05-09-2005	REPRINT	

4. TITLE AND SUBTITLE
Structure in Middle and Upper Atmospheric Infrared Radiance

5a. CONTRACT NUMBER

5b. GRANT NUMBER

5c. PROGRAM ELEMENT NUMBER
62601F

6. AUTHOR(S)
James H. Brown[1], Robert R. O'Neil[1], Richard H. Picard[1], William A.M. Blumberg[1], Edmond M. Dewan[1], Neil A. Grossbard[2] and John H. Gruninger[3]

5d. PROJECT NUMBER
2301

5e. TASK NUMBER
BD

5f. WORK UNIT NUMBER
A1

7. PERFORMING ORGANIZATION NAME(S) AND ADDRESS(ES)

Air Force Research Laboratory
29 Randolph Road
Hanscom AFB, MA 01731-3010

8. PERFORMING ORGANIZATION REPORT NUMBER

AFRL-VS-HA-TR-2005-1114

9. SPONSORING / MONITORING AGENCY NAME(S) AND ADDRESS(ES)

10. SPONSOR/MONITOR'S ACRONYM(S)
AFRL/VSBYB

11. SPONSOR/MONITOR'S REPORT NUMBER(S)

12. DISTRIBUTION / AVAILABILITY STATEMENT
Approved for Public Release; Distribution Unlimited.

[1] Air Force Research Laboratory, Hanscom AFB, MA
[2] Spectral Sciences Inc., Burlington, MA
[2] Boston College, Chestnut Hill, MA

13. SUPPLEMENTARY NOTES
Reprinted from: Proceedings of SPIE Vol. 4539 (2002), Pages 431 - 445

14. ABSTRACT

An extensive database on spatial structure in the infrared radiance of the middle and upper atmosphere has been collected by the Mid-Course Space Experiment (MSX). The observed radiance contains spatial structure down to the scale of hundreds of meters. This spatial structure results from local fluctuations in the temperature and densities of the radiating states of the emitting molecular species as well as fluctuations in radiation transport from the emitting regions to the observer. A portion of this database has been analyzed to obtain statistical parameters characterizing stochastic spatial structure in the observed radiance. Using simple models, the observed statistics have been shown to agree with prior observations and theoretical models of stochastic spatial structure generated by gravity waves for special viewing geometries. The SHARC model has been extended to predict the statistics of stochastic fluctuations in infrared radiance from the statistics characterizing temperature fluctuations in the middle and upper atmosphere for arbitrary viewing geometries. SHARC model predictions have been compared with MSX data and shown to be in generally good agreement. Additional work is in progress to account for the statistics characterizing small spatial scale fluctuations.

15. SUBJECT TERMS
Middle and upper atmosphere; Spatial structure; Gravity waves; Mid-Course Space Experiment; SHARC

16. SECURITY CLASSIFICATION OF:			17. LIMITATION OF ABSTRACT	18. NUMBER OF PAGES	19a. NAME OF RESPONSIBLE PERSON
a. REPORT	b. ABSTRACT	c. THIS PAGE			Richard H. Picard
UNCLAS	UNCLAS	UNCLAS	SAR	15	19b. TELEPHONE NUMBER *(include area code)* 781-377-2222

Structure in Middle and Upper Atmospheric Infrared Radiance

James H. Brown[a], Robert R. O'Neil[a], Richard H. Picard[a], William A.M. Blumberg*[a], Edmond M. Dewan[a], Neil A. Grossbard[b], and John H. Gruninger[c]
[a]Air Force Research Laboratory; [b]Boston College, [c]Spectral Sciences Inc.

ABSTRACT

An extensive database on spatial structure in the infrared radiance of the middle and upper atmosphere has been collected by the Mid-Course Space Experiment (MSX). The observed radiance contains spatial structure down to the scale of hundreds of meters. This spatial structure results from local fluctuations in the temperature and densities of the radiating states of the emitting molecular species as well as fluctuations in radiation transport from the emitting regions to the observer. A portion of this database has been analyzed to obtain statistical parameters characterizing stochastic spatial structure in the observed radiance. Using simple models, the observed statistics have been shown to agree with prior observations and theoretical models of stochastic spatial structure generated by gravity waves for special viewing geometries. The SHARC model has been extended to predict the statistics of stochastic fluctuations in infrared radiance from the statistics characterizing temperature fluctuations in the middle and upper atmosphere for arbitrary viewing geometries. SHARC model predictions have been compared with MSX data and shown to be in generally good agreement. Additional work is in progress to account for the statistics characterizing small spatial scale fluctuations.

Keywords: Middle and upper atmosphere, infrared, spatial structure, gravity waves, Mid-Course Space Experiment, SHARC

1. INTRODUCTION

Gravity waves play a critical role in determining the structure of the lower and middle atmosphere and also play a key role in determining the spatial structure of the radiance of the upper atmosphere. Small scale waves are a dominant source of the transport of atmospheric energy and momentum[1,2]. A new and important data base on gravity waves in the middle and upper atmosphere has been collected by the Mid-Course Space Experiment (MSX)[3,4]. The first space-based mid-wave infrared (MWIR) observations of gravity waves were made using the narrow band MWIR sensor on MSX[5]. Circular gravity waves generated by a thunderstorm cell have also been observed by MSX[6]. The extensive MSX data base on spatial structure in atmospheric radiance has now been analyzed to determine statistics characterizing stochastic spatial structure in the radiance of the middle and upper atmosphere. Theoretical approaches for relating the power spectral densities (PSDs) of the observed radiance fluctuations to the underlying temperature and density fluctuations have been developed. The inferred temperature statistics have been compared both to prior measurements and theoretical accounts of the statistics of temperature and wind velocity fluctuations caused by gravity waves in the stratosphere and mesosphere.

2. MSX OBSERVATIONS OF SPATIAL STRUCTURE IN MIDDLE AND UPPER ATMOSPHERIC RADIANCE

2.1 The Mid-Course Space Experiment (MSX)

The MSX satellite was launched into a 900 km altitude, nearly sun-synchronous, circular polar orbit. A key mission goal was collecting data on the spatial structure in the radiance of the middle and upper atmosphere using the SPIRIT-3 radiometer. The six wavelength channels of the SPIRIT-3 sensor included the B1 band (4.22-4.36 μm) which was selected to collect data on atmospheric radiance in the heart of the 4.3 μm CO_2 absorption band. The contributions to radiance observed in the B1 band come from altitudes above 20 km due to optical opacity effects. B1 band data was

* william.blumberg@hanscom.af.mil; phone 781-377-2951; fax 781-377-5688; Air Force Research Lab/VSB, 29 Randolph Road, Hanscom AFB, MA 01731

Remote Sensing of Clouds and the Atmosphere VI, Klaus Schäfer, Olga Lado-Bordowsky, Adolfo Comeron, Michel R. Carleer, Janet S. Fender, Editors, Proceedings of SPIE Vol. 4539 (2002) © 2002 SPIE · 0277-786X/02/$15.00

collected for a wide variety of viewing geometries including below the horizon (BTH) near-nadir and near limb as well as above the horizon (ATH) viewing geometries. Sensor saturation effects limited data collected on atmospheric radiance from O_3 in the SPIRIT-3 A band (6.8-10.8 μm) to ATH viewing geometries with tangent heights above 55 km. Each radiometer channel consisted of two or more staggered linear arrays of 192 pixels each having a field of view of 90 μrad (the B band was divided into B1 and B2 bands each consisting of two rows of approximately 86 pixels, respectively). The spatial resolution was 80 and 300 m per pixel for nadir and earth limb views, respectively. The data presented here was collected in a push broom scan mode with the detector arrays oriented perpendicular to the spacecraft velocity as illustrated in Fig.1. Great care was put into pre-launch and on-orbit calibration of the SPIRIT-3 sensors, and the uncertainty in the absolute radiances measured by the SPIRIT-3 radiometer is less than 10%. IR data collections were conducted using the cryogenic SPIRIT-3 sensors on MSX from 24 April 1996 until 25 February 1997.

2.2 MSX data collections used

Data presented in this paper was collected using the MSX SPIRIT-3 B1 and A bands for a variety of viewing geometries. BTH and ATH data collected in the narrow MWIR B1 band was analyzed to determine the effects of temperature and density fluctuations on radiance from CO_2. ATH data collected in the long wave infrared (LWIR) A band was also analyzed to determine temperature and density effects on O_3 radiance fluctuations for comparison purposes. For this analysis the following BTH scene data was used:

	Band	Nadir Angle	Scene Dimensions
Scene 1	B1	1.3^0	6.7 x 2701 km^2
Scene 2	B1	55^0	13.5 x 1164 km^2
Scene 3	B1	57^0	15.1 x 4237 km^2

In addition, the following ATH scene data was analyzed:

	Band	Tangent Height	Scene Dimensions
Scene 4	B1	1.8 – 16 km	14.2 x 1050 km^2
Scene 5	B1	40 – 54 km	14.0 x 1367 km^2
Scene 5A	A	57.3 – 71.2 km	13.9 x 1063 km^2

The MSX line of sight and tangent point ground tracks for these data collections are shown in Fig 2. Shown in Fig. 3 are the six MSX scenes used for the present analysis of atmospheric structure.

2.3 MSX scene data analysis

The six MSX scenes described above were analyzed to obtain a variety of descriptors of the spatial content of the scenes. The scene data was sufficiently over-sampled during collection to maintain the spatial resolution inherent in the sensor footprint and to avoid aliasing effects. Average radiance and relative standard deviation profiles derived from the pixel time histories are shown in Fig. 4. The relative standard deviation profiles include both deterministic and gravity wave induced stochastic structure and thus set an upper limit on the stochastic structure in the scenes.

Data over-sampling permitted decimation and co-adding of data samples in the in-scan direction to improve signal to noise and thus the power spectral densities (PSDs) derived from the data. To determine the statistical parameters characterizing the scenes, each scene was de-trended by subtracting a first or second order polynomial fit to the radiance for each row in the scene. Shown in Fig. 5 is a segment of the de-trended scenes presented with unity aspect ratio (equal distance scales in the in-scan and cross-scan directions). As the viewing geometry changes from nadir viewing to limb viewing the spatial structure in the de-trended scenes changes from isotropic to striated.

Both classical and modern spectral analysis techniques were used to estimate PSD functions as a function of wave number (km^{-1}) for the observed stochastic radiance structure. Averaged periodograms of the structure data were generated using the standard techniques of pre-whitening the data[7], applying a Hanning data window[8], and post-coloring the periodogram[9]. Spectral noise was reduced by computing separate periodograms for each column and row of each de-

trended scene and averaging the sets of row and column periodograms, respectively. Modern spectral analysis techniques were also used in which Burg's method[8,9] was used to estimate the coefficients of an auto-regressive (AR) PSD function. Prior to computing PSDs, a number of steps were taken to reduce the non-stationarity of the data. Each scene was de-trended, as described above. Then the de-trended values for each row were divided by the standard deviation for the row and multiplied by the average standard deviation for the entire scene. Since the data are non-stationary in the cross-scan direction, cross scan data were limited to 45 pixels for ATH data and 41 or 84 pixels for BTH data. The in-scan and cross-scan periodogram and auto-regressive PSDs for the six scenes are shown in Figs. 6 and 7. The in-scan (horizontal) large spatial scale PSD slopes are ~ -5/3 for nadir viewing geometries and ~ - 8/3 for limb viewing geometries. The in-scan PSD curves exhibit a change in slope at a spatial scale of 10 km. The cross-scan PSD slopes are ~ -4 for limb viewing geometries.

2.4 Consistency of MSX radiance observations with observations and prior theory of gravity waves

Prior observations of gravity waves show temperature and wind velocity PSDs generally varying as $k_x^{-5/3}$ [10], although there is evidence of k_x^{-3} behavior at small spatial scales between 1 and 10 km under some conditions[11,12,13,14,15,16,17,18,19,20], and k_z^{-3} [21,22,23], where k_x and k_z are wavenumbers in horizontal and vertical directions. A number of theories of gravity waves also predict temperature and wind velocity PSDs varying as $k_x^{-5/3}$ and k_z^{-3} [23,24,25,26,27,28,29,30,31,32,33,34,35]. However, the SPIRIT-3 sensor on MSX measures radiance observed along lines of sight, not in-situ temperature or wind velocity. Calculations of radiative contribution functions for atmospheric 4.3 μm radiance show that the observed MWIR radiance in the B1 band comes from a narrow range of altitudes around 40 km. The nadir to limb viewing observations made by MSX span a wide range of ratios of path length in the radiating layer to the spatial scale of atmospheric temperature fluctuations. A model calculation of the effects of integrating through an isotropic two dimensional fluctuation field (displayed in Fig 8) shows that the PSD changes by a factor of k^{-1} when the path length in the radiating layer is on the order of 2 to 3 correlation lengths. The steepening of the PSD slope can be understood as the result of the low-pass filtering resulting from the integration along the line of sight. This result suggests that the change in the slopes of the large spatial radiance PSDs observed by MSX from –5/3 for nadir viewing geometries to –8/3 for limb viewing geometries is a filtering effect due to observing a fluctuating layer of fixed thickness along a slant path. A parallel argument applies to why the slopes of the small spatial scale, cross-scan (near vertical in the BTH near-limb and ATH scans) radiance PSDs are observed to be –4, as opposed to –3 which would be expected for the k_z dependence of the temperature spectrum. However a detailed atmospheric model is required to relate temperature and density fluctuation spectra in the middle and upper atmosphere to observed radiance fluctuation spectra for arbitrary viewing conditions.

3. SHARC MODEL FOR STOCHASTIC SPATIAL STRUCTURE

3.1 Introduction

The Air Force Research Laboratory originally developed the SHARC model[36] to describe line of sight spectra, in-band radiance, and transmittance in the middle and upper atmosphere. A key feature of the SHARC model is that it describes non-local thermodynamic equilibrium (NLTE) effects on the populations of radiating molecular vibrational states, which is important for all species above some altitude in the middle and upper atmosphere but not important in the lower atmosphere. The SHARC model has subsequently been extended to include stochastic spatial structure due to superposed and interacting atmospheric gravity waves[37,38]. A key challenge is developing a computationally tractable method for relating temperature and density fluctuations in a sensor field of view to the fluctuations in the radiance in the image plane of the sensor. SHARC provides the capability for predicting scene spatial structure in atmospheric radiance in the wavelength range 2-40 μm for arbitrary viewing geometries as long as there is no significant contribution to the radiance from altitudes below 30 km. Thus the SHARC model is appropriate for predicting stochastic spatial structure observed by MSX in the B1 band for the full range of viewing geometries and for structure observed in the MSX A band for tangent heights above 30 km. As will be shown below, SHARC model predictions of radiance PSDs are consistent with analytic solutions from gravity wave theory for special limiting cases (nadir and horizontal viewing geometries). The model predictions are also consistent with the MSX MWIR observations of large-scale BTH stochastic spatial structure and of small-scale stochastic structure observed for ATH lines of sight.

The inputs to the new SHARC model for stochastic spatial structure are the data base of the altitude profiles of kinetic temperature and atomic and molecular species densities provided by the SHARC Atmospheric Generator (SAG)[43], the data base on molecular spectral line parameters provided by HITRAN-92[44], and a model of three dimensional structure

describing the atmospheric temperature fluctuation spectra and autocovariance functions. The PSDs are assumed to be separable into horizontal and vertical components, and the altitude dependence of temperature fluctuation correlation lengths and variance is provided by Strugala et. al.[39]. The SHARC spectral model is used to calculate the populations of the vibrational levels of radiating species under NLTE conditions and the resulting radiance spectra and in-band radiance as a function of the line of sight. The SHARC spatial structure model generates radiance autocovariance contribution functions, which enable one to calculate radiance PSDs, variances and correlation lengths for non-stationary stochastic radiance fluctuations due to gravity waves.

3.2 Details of the SHARC structure model calculation

If temperature fluctuations, $\Delta T(\vec{r})$, are sufficiently small that linear response can be assumed, the radiance fluctuations, $L_{\Delta\lambda}(\vec{p})$, in the pass band, $\Delta\lambda$., in an image plane can be expressed as an integral along the line of sight of the line of sight radiance response function, $F_{\Delta\lambda}(\vec{r})$, which accounts for all path-integration and geometrical filtering effects, times the atmospheric kinetic temperature fluctuations, $\Delta T(\vec{r})$:

$$\Delta L_{\Delta\lambda}(\vec{p}) = \int dr\, F_{\Delta\lambda}(\vec{r})\Delta T(\vec{r}). \tag{1}$$

Here, the vector, $\vec{p}$, defines the pixel location in the image plane, and $\vec{r}$ is the position vector of the pixel $\vec{p}$ relative to the source point. It has been assumed that dynamical fluctuations are adiabatic, so that density fluctuations can be expressed simply in terms of temperature fluctuations. In the case of species and conditions where NLTE effects are important, $F_{\Delta\lambda}(\vec{r})$ includes contributions from all kinetic temperature fluctuations, including those which enter through the dependence of the vibrational temperatures characterizing the populations of the radiating state on kinetic temperature. In general, it is possible for the radiative transport of temperature fluctuations in regions not on the line of sight to produce additional radiance fluctuations along the line of sight. Then equation (1) becomes a volume integral rather than a line integral. We will specifically exclude such nonlocal effects in this paper, although it is possible that they might play some role in Scenes 5 and 5A.

The radiance autocovariance function, $Cov_L(\vec{p},\vec{p}')$, can be expressed as $Cov_L(\vec{p},\vec{p}') = E[\Delta L_{\Delta\lambda}(\vec{p})\Delta L_{\Delta\lambda}(\vec{p}')]$ where $\vec{p}$ and $\vec{p}'$ point to two locations in the sensor image and E[x] is the expectation value of x. From equation (1), $Cov_L(\vec{p},\vec{p}')$ can then be expressed in terms of line of sight integrations of the atmospheric temperature autocovariance function, $Cov_T(\vec{r},\vec{r}')$;

$$Cov_L(\vec{p},\vec{p}') = \int dr\left[\int dr' F_{\Delta\lambda}(\vec{r})F_{\Delta\lambda}(\vec{r}')Cov_T(\vec{r},\vec{r}')\right]. \tag{2}$$

Here $\vec{r}$ and $\vec{r}'$ are two line of sight vectors that point to the $\vec{p}$ and $\vec{p}'$ end points in the image plane. The quantity in square brackets is the line of sight autocovariance contribution function, $W_L(\vec{r},\vec{p},\vec{p}')$, so that $Cov_L(\vec{p},\vec{p}') = \int dr W_L(\vec{r},\vec{p},\vec{p}')$. Under conditions of local stationarity where the characteristic spatial scales of the fluctuating quantities is small compared to the scale over which the mean values of these quantities change (for example, the vertical temperature correlation length is much less than the atmospheric scale height), the expressions for the radiance and temperature autocovariance functions depend strongly only upon the displacements $\Delta\vec{p} = \vec{p} - \vec{p}'$ and $\Delta\vec{r} = \vec{r} - \vec{r}'$.

Under conditions of local stationarity, taking the Fourier transform of equation (2) leads to a simple relation between the radiance PSD and the three dimensional temperature PSD:

$$PSD_L(\vec{p},k_v,k_h) = \int dr\left[\frac{1}{2\pi}\int dk_{los} e^{ik_{los}r} F_{\Delta\lambda}(\vec{r})Q_{\Delta\lambda}(k_{los})PSD_T(\vec{r},k_{los},k_v,k_h)\right], \tag{3}$$

where $Q_{\Delta\lambda}(k_{los})$ is the Fourier transform of the LOS radiance response function, $F_{\Delta\lambda}(\vec{r}')$, k_{los} is the spatial wave number along the LOS, k_v and k_h are the "sensor vertical" and "sensor horizontal" wave numbers respectively, and where the sensor horizontal direction is the direction in the image plane parallel to the horizon and the sensor vertical direction is perpendicular to both the sensor horizon and the line of sight. If the atmospheric temperature PSD is stationary over

that portion of the line of sight which contributes to the radiance then the dependence of the radiance PSD on range along the line of sight can be neglected, and equation (3) can be re-written, after integrating over r,

$$PSD_L(k_v,k_h)=\frac{1}{2\pi}\int dk_{los}\left|Q_{\Delta\lambda}(k_{los})\right|^2 PSD_T(k_{los},k_v,k_h). \tag{4}$$

Here $\left|Q_{\Delta\lambda}(k_{los})\right|^2$, the path-integration filter in spatial-frequency space, is the square of the magnitude of the Fourier transform of the line of sight radiance response function.

As described above, a key input to the SHARC stochastic radiance model is the three dimensional temperature autocovariance function. Assuming that the temperature autocovariance function is separable into horizontal (h=(x,y)) and vertical (z) components, then $Cov_T(\vec{r},\Delta\vec{r})=Cov_H(\vec{r},\Delta H)Cov_z(\vec{r},\Delta z)$, and the corresponding three-dimensional PSD is also separable and can be expressed as: $PSD_T(\vec{r},\vec{k})=PSD_H(\vec{r},k_H)PSD_z(\vec{r},k_z)$. The von Karman spectral model[40,41,42] is used here to model the atmospheric vertical and horizontal power spectra and autocovariance functions. The vertical temperature PSD and autocovariance functions are given by:

$$PSD_z(\vec{r},k_z)=N_z\sigma_T^2(\vec{r})\ell_z(\vec{r})(1+\ell_z^2(\vec{r})k_z^2)^{-(\nu_z+1/2)} \tag{5}$$

and

$$Cov_z(\vec{r},\Delta z)=M_z\sigma_T^2(\vec{r})(\Delta z/\ell_z(\vec{r}))^{\nu_z}K_{\nu_z}(\Delta z/\ell_z(\vec{r})). \tag{6}$$

Similarly, the horizontal temperature PSD and autocovariance functions are given by:

$$PSD_H(\vec{r},k_H)=N_H\sigma_T^2(\vec{r})\ell_H^2(\vec{r})(1+\ell_H^2(\vec{r})k_H^2)^{-(\nu_H+1)} \tag{7}$$

and

$$Cov_H(\vec{r},\Delta H)=M_H\sigma_T^2(\vec{r})(\Delta H/\ell_H(\vec{r}))^{\nu_H}K_{\nu_H}(\Delta H/\ell_H(\vec{r})). \tag{8}$$

where $\ell_H^2(\vec{r})=\ell_x^2(\vec{r})+\ell_y^2(\vec{r})$, $k_H^2=k_x^2+k_y^2$, and $\Delta H^2=\Delta x^2+\Delta y^2$. Here K_{ν_z} and K_{ν_H} are modified Bessel functions of the second kind of order ν_z and ν_H, respectively, and N_z, M_z, N_H, and M_H are normalization constants. The temperature variance, $\sigma_T^2(\vec{r})$, vertical scale length, $\ell_z(\vec{r})$, and horizontal scale length, $\ell_H(\vec{r})$, depend parametrically on $\vec{r}$ as the LOS continuously changes altitude. Values for the scale lengths and temperature variances have been taken from *Strugala et al*[39].. By selecting the Bessel function orders ν_z and ν_H as 1 and 1/3 respectively, the asymptotic vertical spectral index at large k_z is –3 and the 2-D asymptotic horizontal spectral index is –8/3, leading to a 1-D horizontal spectral index of –5/3. The model is consistent with simple gravity wave model predictions and observations for spatial wave number regions where the vertical index is –3 and the 1-D horizontal index is –5/3. The assumption of separability in k_x and k_z is a reasonable approximation for the case of multiple superposed gravity waves as opposed to a single gravity wave.

Because of the non-stationarity and the lack of vertical-horizontal isotropy, observational effects on radiance PSD slopes due to line-of-sight integration are a function of the relative vertical and horizontal scale lengths and the orientation of LOS through the atmospheric structure. There are two special orientations for which analytical results can be obtained. The first situation where one can obtain an analytic solution is pure nadir or zenith viewing, in which the LOS integration is in the vertical and hence independent of horizontal structure. There is no steepening of the radiance PSD spectral slope, and nadir views through the separable gravity wave model have a radiance PSD with a spectral slope close to –5/3. The second situation where analytic solutions are possible is pure horizontal viewing, in which the LOS passes through the isotropic horizontal structure. The 1-D horizontal wave number spectral slopes steepen with the index changing from –5/3 to –8/3 [38]. Limb viewing often approximates pure horizontal viewing since the limb path is essentially a horizontal path at the tangent point. It was shown[38] that for power law type PSDs, the magnitude of the spectral index increases by one. Hence, for limb viewing, when the radiance band is sufficiently optically thin that the contributions come primarily from the tangent point altitude, the vertical power spectral index is essentially unaffected and the one dimensional horizontal index changes from -5/3 to –8/3. The LOS integration also transforms the order of the modified Bessel functions occurring in the radiance autocovariance function. The order is increased by ½ corresponding to the spectral index changing from $-n$ to $-(n+1)$.

4. DATA-MODEL COMPARISONS

4.1 Comparisons of Radiance and Their Relative Standard Deviations

The full SHARC model was used to predict radiances and standard deviations of stochastic fluctuations in radiance for the six MSX scenes described in Section 2.2. Measured and predicted radiances, as well as relative measured and predicted standard deviations of the stochastic component of radiance are shown in Table 1. The measured and predicted radiances agree within the uncertainties of the model altitude profiles of temperature. All discrepancies are accounted for by temperature adjustments of about 5 K at 40 km. However, the predicted relative standard deviations for radiance fluctuations are significantly larger than the relative standard deviations obtained from the six MSX scenes. The predicted standard deviations, of course, reflect the temperature variance database in the model[39]. Analysis of the extensive MSX scene database will provide additional inputs for adjusting the temperature variance database.

4.2 Radiance PSD Comparisons

The principal contributions to radiance fluctuations in the narrow 4.3 μm B1 band for the viewing geometries of Scenes 1 – 4 come from an atmospheric layer with maximum contribution at 40 km. In addition, day lit portions of viewing lines of sight also have NLTE contributions from the 65 to 80 km altitude range arising from solar-excited fluorescent emissions. Shown in Fig. 9 is the LTE portion of the radiance variance contribution function calculated for the conditions of Scenes 1 and 3. The contribution function is slightly broader for nadir than for sub-limb viewing.

When contributions from broad or multiple layers are present, the non-stationarity of the temperature and density structure of the atmosphere needs to be taken into account. The effect of path integration is to act as a low pass filter. Thus the radiance PSDs can be expected to have a steeper fall off with wave number than do the underlying temperature PSDs for viewing geometries where the line of sight passes obliquely through a radiating layer or lies nearly horizontal to it. The dependence of the radiance PSD spectral index on the local zenith angle (LZA), or angle that the line of sight makes with the radiating layer at 40 km for the in-scan and cross-scan directions, is shown in Figs. 10 and 11 for two ratios of horizontal to vertical temperature correlation lengths. The slope of the PSD varies from –5/3 to –8/3 in the in-scan direction and from –5/3 to –4 in the cross-scan direction, as has been described above. Also shown are the in-scan radiance spectral slopes obtained from MSX scenes 1 to 5A for spatial scales > ~10 km, which agree reasonably well with the model predictions. The model predictions for the slopes of the cross-scan radiance PSDs also agree well with the measured PSD slopes shown in Fig. 7.

5. CONCLUSIONS

Unique data on the spatial structure of the radiance of the middle and upper atmosphere has been collected using the SPIRIT-3 radiometer on MSX. The radiance fluctuation observations made by MSX are consistent with stochastic spatial structure resulting from atmospheric gravity waves. The SHARC model used to predict infrared spectra, in-band radiance, and transmittance in the middle and upper atmosphere has been extended to predict stochastic spatial structure due to gravity waves. The SHARC predictions of stochastic spatial structure agree relatively well with the MSX data for large-scale spatial structure (scale lengths > ~10 km). A new capability is the ability to relate the variances and PSDs of infrared radiance in the middle and upper atmosphere for arbitrary viewing geometries to the variances and PSDs describing atmospheric temperature fluctuations. With this capability the extensive MSX database on spatial structure in the atmospheric radiance can be fully exploited to characterize the temperature structure of the middle and upper atmosphere. Additional work is in progress to account more fully for the small-scale spatial structure observed by MSX.

ACKNOWLEDGEMENTS

We acknowledge the key support for MSX data analysis made by H. Gardiner, J. Duff, E. Richards, and E. R. Hegblom and the entire MSX team. RHP gratefully acknowledges support from Dr. Kent Miller of the Air Force Office of Scientific Research.

REFERENCES

1. D. C. Fritts, and T. E. VanZandt, Spectral estimates of gravity wave energy and momentum fluxes. Part I: Energy dissipation, acceleration, and constraints, *J. Atmos. Sci.*, *50*, 3685-3694, 1993.
2. D. C. Fritts, and W. Lu, Spectral Estimates of gravity wave energy and momentum fluxes. Part II: Parameterization of wave forcing and variability, *J. Atmos. Sci.*, *50*, 3695-3700, 1993.
3. J. Mill, R. O'Neil, S. Price, G. Romick, O. Ul, and E. Gaposchkin, Midcourse Space Experiment: Introduction to the spacecraft, instruments, and scientific objectives, *J. Spacecraft & Rockets*, *31*, 900-907, 1994.
4. R. R. O'Neil, H. A. B. Gardiner, J. Gibson, C. Humphrey, R. Hegblom, M. E. Fraser, M. Kendra, P. Wintersteiner, and C. Rice, Midcourse Space Experiment (MSX), *Proc. Soc. Photo. Opt. Instrum., Eng.*, *2223*(25), 264-273, 1994.
5. R. H. Picard, R. R. O'Neil, H. A. Gardiner, J. Gibson, J. R. Winick, W. O. Gallery, A. T. Stair, P. P. Wintersteiner, E. R. Hegblom, and E. Richards, Remote sensing of discrete stratospheric gravity-wave structure at 4.3-μm form the MSX satellite, *Geophys. Res. Lett.*, *25*, 2809-2812, 1998.
6. E. M. Dewan, R. H. Picard, R. R. O'Neil, H. A. Gardiner, J. Gibson, J. D. Mill, E. Richards, M. Kendra, and W. O. Gallery, MSX satellite observations of thunderstorm-generated gravity waves in mid-wave infrared images of the upper stratosphere, *Geophys. Res. Lett.*, *25*, 939-942, 1998.
7. R. B. Blackman, and J. W. Tukey, *The measurement of power spectra: From the point of view of communications engineering*, Dover Publications, New York, 1958.
8. S. L. Marple, *Digital spectral analysis with applications*, Prentice-Hall, 213, 1987.
9. D. B. Percival and A. T. Walden, *Spectral analysis for physical applications: Multitaper and conventional univariate techniques*, Cambridge Univ. Press, Cambridge, U.K., 1993.
10. G. D. Nastrom and K. S. Gage, A first look at wave number spectra from GASP data, *Tellus*, *35A*, 383-388, 1983.
11. G. N. Shur, Experimental investigations of the energy spectrum of atmospheric turbulence [in Russian], *Tr. Tsentra. Aerolog. Observ.*, *43*, 79-90, 1962.
12. G N. Shur, Aircraft investigation of clear air turbulence in the troposphere and stratosphere. in *Proceedings of the All-Union Conferences on Questions of Meteorological Support for Supersonic Aviation* pp. 141-149 [in Russian], Izd. LGMI, Moscow, 1971.
13. B. M. Koprov, Spectra of turbulent vertical velocity component in the atmospheric boundary layer at the convection conditions, [in Russian] *Akad. Nauk. SSSR, Izv., Fiz. Atmos. i Okeana*, *1*(11), 1151-1159, 1965.
14. N. K. Vinnichenko, N. Z. Pinus, and G. N. Shur, Some results of the experimental turbulence investigations in the troposphere, in Atmospheric Turbulence and Radio Wave Propagation (Proceedings of the International Colloquium, Moscow 1965), [partly in Russian], A. M. Yaglom and V. I. Tatarskii, editors, Nauka, Moscow, 1967.
15. L. O. Myrup, Atmospheric measurements of the buoyant subrange of turbulence, *J. Atmos. Sci.*, *25*, 1160-1164, 1968.
16. L. O. Myrup, Turbulence spectra in stable and convective layers in the free atmosphere, *Tellus 21 (3)*, 341-354, 1969.
17. D. K. Lilly and P. F. Lester, Waves and turbulence in the stratosphere, *J. Atmos., Sci.*, *31*, 800-812, 1974.
18. E. A. Berman, Measurements of temperature and downwind spectra in the "buoyant subrange", *J. Atmos. Sci.*, *33*, 495-498, 1976.
19. G. D. Nastrom, D. C. Fritts, and K. S. Gage, An investigation of terrain effects on the mesoscale spectrum of atmospheric motions, *J. Atmos. Sci.*, *44*, 3087-3096, 1987.
20. J. T. Bacmeister, S. D. Eckermann, P. A. Newman, L. Lait, K. R. Chan, M. Loewenstein, M. H. Proffitt, and B. L. Gary, Stratospheric horizontal wavenumber spectra of winds, potential temperature, and atmospheric tracers observed by high-altitude aircraft, *J. Geophys. Res.*, *101*(D5), 9441-9470, 1996.
21. T. VanZandt, A universal spectrum of buoyancy waves in the atmosphere, *Geophys. Res. Lett.*, *9*, 575-578, 1982.
22. E. M. Dewan and R. E. Good, Saturation and the universal spectrum for vertical profiles in the stratosphere, *J. Geophys. Res.*, *91*(D2), 2742-2748, 1986.
23. S. D. Smith, D. Fritts, and T. VanZandt, Evidence for a saturated spectrum of atmospheric gravity waves, *J. Atmos. Sci.*, *44*, 1404:1410, 1987.
24. E. M. Dewan and R. E. Good, Saturation and the universal spectrum for vertical profiles in the stratosphere, *J. Geophys. Res.*, *91*(D2), 2742-2748, 1986.
25. E. M. Dewan, Similitude modeling of internal gravity wave spectra, *Geophys. Res. Lett, 18*, 1473-1476, 1991.
26. E. M. Dewan, The saturated-cascade model for atmospheric gravity wave spectra, and the wavelength-period (W-P) relations, *Geophys. Res. Lett.*, *21*, 817-820, 1994.
27. E. M. Dewan, Saturated-cascade similitude theory of gravity wave spectra, *J. Geophys. Res.*, *102*-(D25), 29799-29817, 1997.
28. C. O. Hines, The saturation of gravity waves in the middle atmosphere, part I: Critique of linear-instability theory, *J. Atmos. Sci.*, *48*, 1348-1359, 1991.
29. C. O. Hines, The saturation of gravity waves in the middle atmosphere, part II: Development of doppler-spread theory, *J. Atmos. Sci.*, *48*, 1360-1379, 1991.

30. C. O. Hines, The saturation of gravity waves in the middle atmosphere, part III: formation of the turbopause and of the turbulent layers beneath it, *J. Atmos. Sci.*, *48*, 1380-1385, 1991c.
31. K. S. Gage, Evidence for a $k^{-5/3}$ law inertial range in mesoscale two-dimensional turbulence, *J. Atmos. Sci.*, *36*, 1950:1954, 1979.
32. K. S. Gage and G. D. Nastrom, Theoretical interpretation of atmospheric wave number spectra of wind and temperature observed by commercial aircraft during GASP, *J. Atmos. Sci.*, *43*, 729-740, 1986.
33. D. K. Lilly, Stratified turbulence and the mesoscale variability of the atmosphere, *J. Atmos., Sci.*, *40*, 749-761, 1983.
34. J. Weinstock, Saturated and unsaturated spectra of gravity waves and scale-dependent diffusion, *J. Atmos. Sci.*, *47*, 2211-2225, 1990.
35. X. Zhu, A new theory of the saturated gravity wave spectrum for the middle atmosphere, *J. Atmos. Sci.*, *51*, 3615-3626, 1994.
36. R. L. Sundberg, J. W. Duff, J. H. Gruninger, L. S. Bernstein, M. W. Matthew, S. Adler-Golden, D. C. Robertson, R. D. Sharma, J. H. Brown, and R. J. Healey, SHARC, A model for calculating atmospheric infrared radiation under non-equilibrium conditions, *The upper mesosphere and lower thermosphere: A review of experiment and theory,* Geophys. Monogr. Series, Vol. *87*, pp. 287-295, American Geophysical Union, D.C., 1995.
37. J. H. Gruninger, R. Sundberg, J. Duff, J. H. Brown, R. Sharma, and R. Sears, Modeling for atmospheric background radiance structures, *Proc. Soc. Photo. Opt. Intrum. Eng.*, *2580*, 1-16, 1995.
38. J. H. Gruninger, J. Duff, J. H. Brown, and W. A. M. Blumberg, Radiation transport effects and the interpretation of infrared images of gravity waves and turbulence, *Proc. Soc. Photo. Opt. Intrum. Eng*, *3495*, 122-135, 1998.
39. L. A. Strugala, R. D. Sears, J. E. Newt, and B. J. Herman, Production of statistically non-stationary stochastic structure realizations for infrared background scene simulations, *Opt. Eng.*, *32*, 993-1001, 1993.
40. R. R. Beland, *Propagation through atmospheric optical turbulence*, Chap. 2 *of The Infrared & Electro-Optical Systems Handbook*, Vol. 2, Atmospheric Propagation of Radiation, F. G. Smith, editor, pg.174, ERIM, SPIE PRESS, Ann Arbor, 1993.
41. V. A. Banakh and V. L. Mironov, *Lidar in a Turbulent Atmosphere*, p. 6, Artech House, Boston, 1987.
42. J. H. Brown, *Atmospheric structure simulation: An autoregressive model for smooth geophysical power spectra with known autocorrelation function*, Phillips Laboratory Technical Report No. *PL-TR-93-2185*, ADA 276691, 1993.
43. S.M. Adler-Golden, *Description of the SHARC Atmosphere Generator*, Phillips Laboratory Technical Report No. *PL-TR-93- 2123*, 1993.
44. L. S. Rothman, R Gamache, A. Goldman, L. R. Brown, R. A. Toth, H. M. Pickett, R. L. Poynter, J.-M. Flaud, C. Camy-Peyret, A. Barbe, N. Husson, C. P. Rinsland, and M. A. H. Smith, The HITRAN molecular database: Editions of 1991 and 1992, *J. Quant. Spectrosc. Radiat. Transfer*, *48*, 469, 1992.

Scene #	Approx. latitude start/end	Local zenith angle @ 40 km alt (deg.)	Tan. Alt. (km)	Measured[1] Radiance (Trend) ($\mu W/cm^2$-sr)	Predicted avg. radiance ($\mu W/cm^2$-sr)	Measured[2] Std. Dev./ Row Avg. %	Measured[3] Std. Dev./ Trend %	Predicted Std. Dev. / Predicted Avg. %
1	12^0N – 35^0N	1.7	BTH/ nadir	.90 – 1.06 .90 – 1.06	1.0 –1.2	1.04 1.21	1.11 – 0.94 1.29 – 1.09	4.9
2	30^0N – 40^0N	78	BTH/ terminator	.77 – .53 .74 – .52	0.94 – 0.78	1.32 1.50	1.11 – 1.61 1.28 – 1.81	5.1 – 5.3
3	19^0N – 55^0N	82	BTH	1.12 – 1.28 1.13 – 1.29	1.3 – 1.6	1.33 1.40	1.41 – 1.23 1.50 – 1.32	4.2
4	60^0N – 52^0N	84 - 85	2 16	1.32 – 1.20 1.35 – 1.24	1.7 – 1.6 1.8 – 1.7	0.95 0.89	0.92 – 1.01 0.86 – 0.94	4.2 – 4.4
5	15^0N – 3^0N	90	40 54	1.33 – 1.44 0.36 – 0.23	1.8 – 1.9 0.31 – 0.34	2.97 5.32	3.04 – 2.81 11.1 – 6.70	3.6 8.2
5A	15^0N – 5^0N	-	57 71	8.67 – 8.77 0.94 – 0.85	10.2 – 9.9 1.5 – 1.4	2.36 1.33	2.44 – 2.44 1.25 – 1.39	4.0 3.0

Table 1. Comparison of predicted versus measured average radiance and the percent relative standard deviation of the radiance for six MSX scenes. Standard deviations are calculated from detrended images.

1. Estimate of the average radiance from trend at 4 corners of the scene.
2. Estimate of the standard deviation of the radiance (removing the trend) / row average (%).
3. Estimate of the standard deviation of the radiance (removing the trend) / trend (%) at 4 corners of the scene.

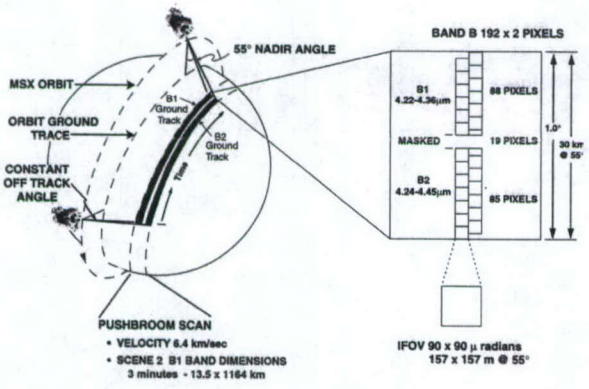

Figure 1. The projection of the MSX focal plane for the MWIR bands, B_1 and B_2, on the lower atmosphere is shown for a case where the line of sight is in a plane orthogonal to the orbit and elevated 55 degrees from the nadir.

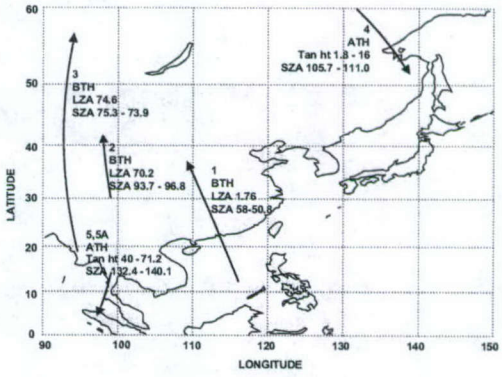

Figure 2. The MSX line of sight target region ground track or tangent point tracks are shown for the below the horizon (BTH) and the above the horizon (ATH) events presented here. The scene number, the local zenith angle (LZA) at the ground for Scenes 1-3 and the tangent altitude (tan ht) for Scenes 4-5 and the solar zenith angles (SZA) are indicated.

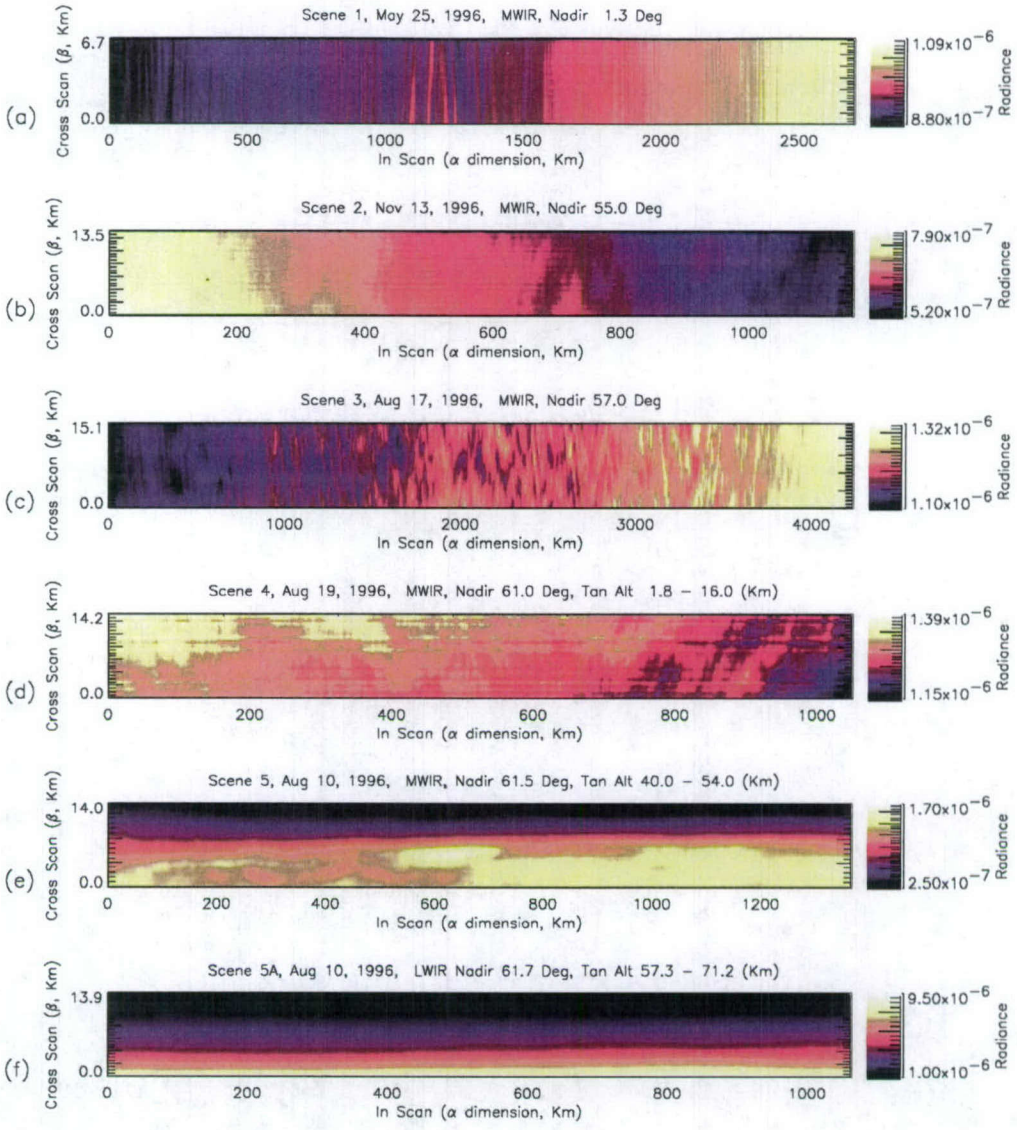

Figure 3. False-color "raw" images for six MSX Scenes. The scenes are obtained from the MSX radiometer "looking" perpendicular to the satellite trajectory at fixed nadir angles (so-called "push-broom" scans). The "cross-scan" to "in-scan" aspect ratios are much less than 1 to allow inspection on the page (images appear compressed in the in-scan dimension).

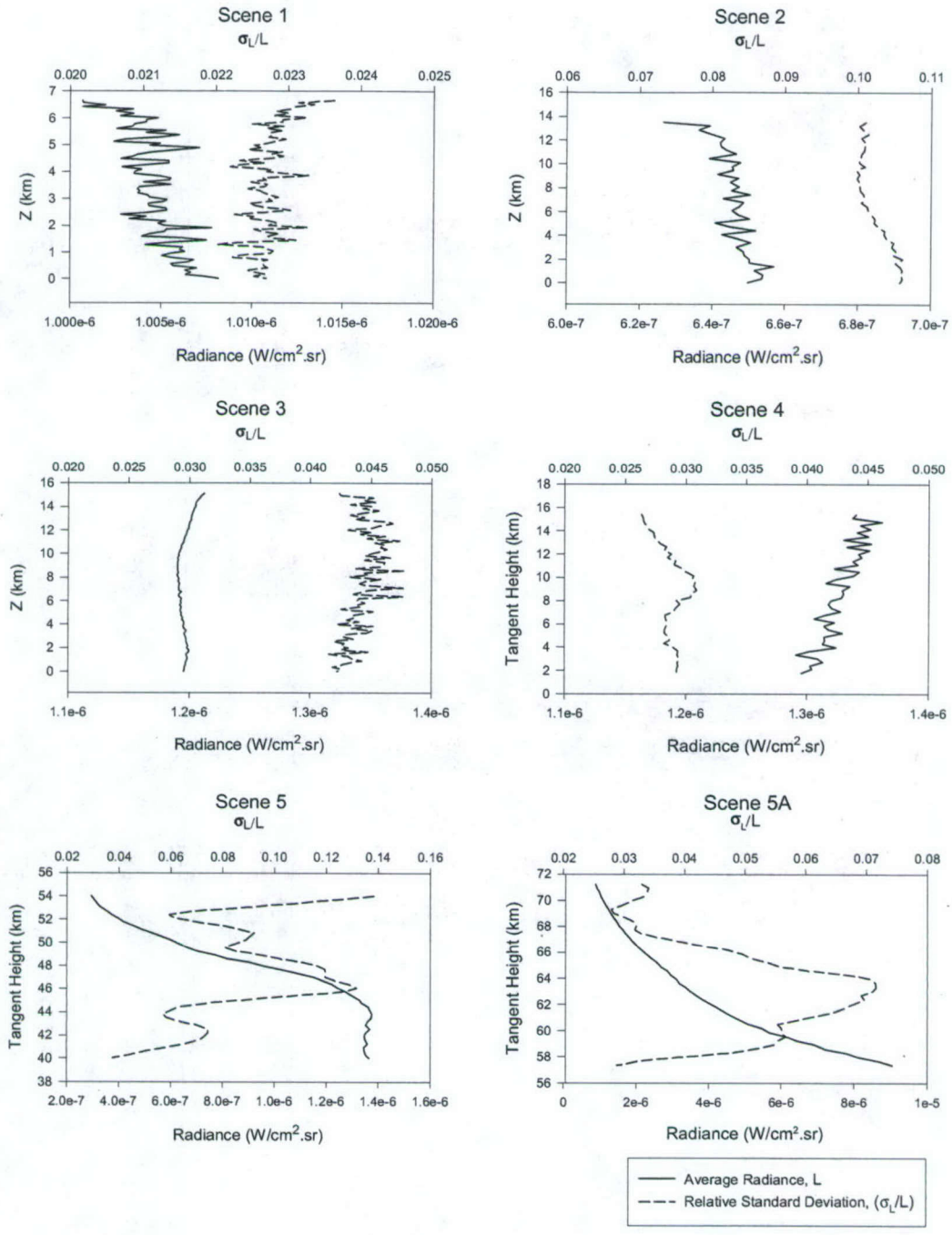

Figure 4. Background radiance and relative standard deviation of radiance for six MSX scenes. "Z" is distance orthogonal to the line-of-sight and parallel to the sensor vertical. The average is computed over the entire length of the scene.

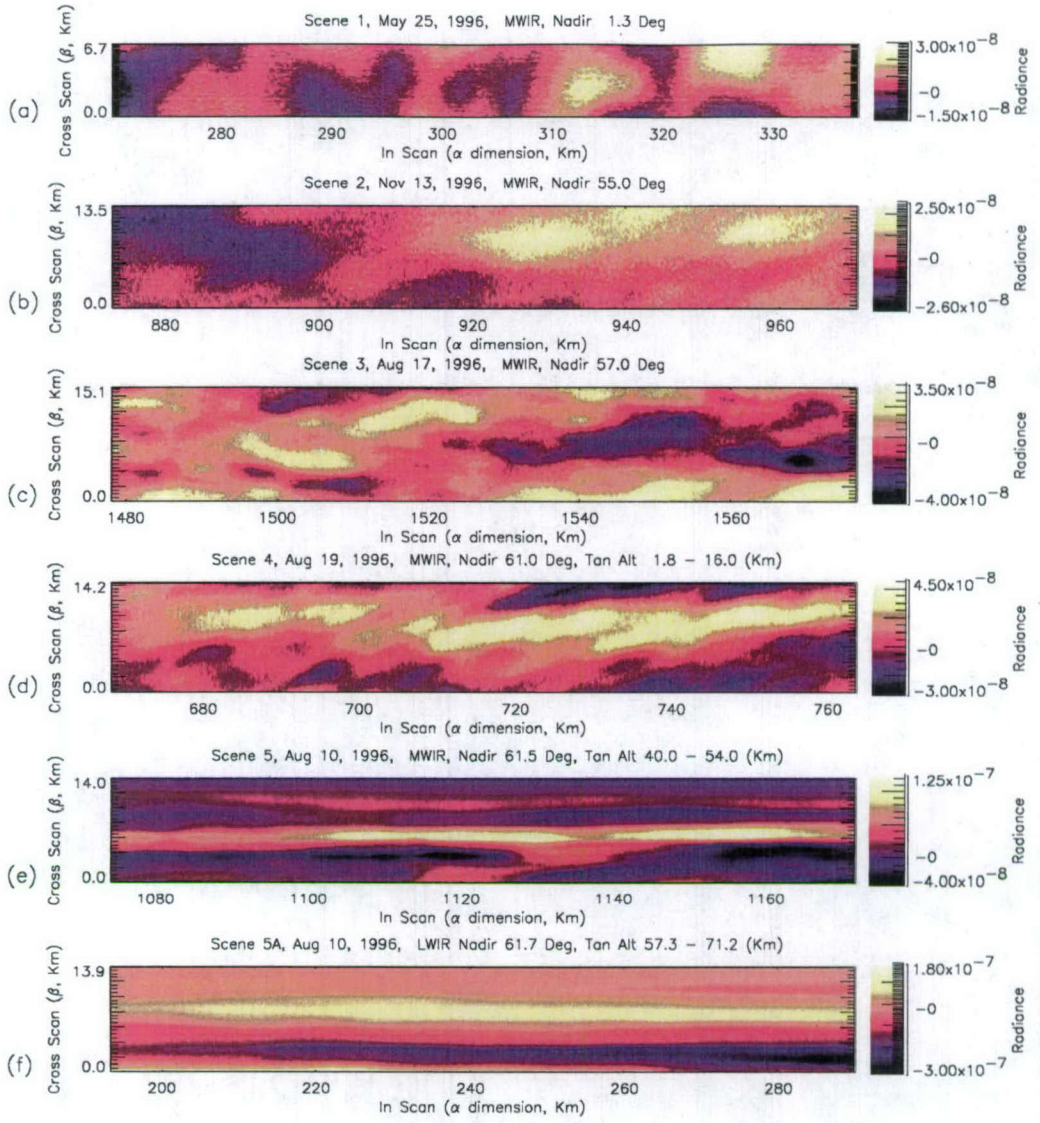

Figure 5. Segments of the false-color "detrended" images from Figure 3. The images show residual perturbations or radiance fluctuations after removing the trends in the in-scan dimension. The images have an aspect ratio = 1.

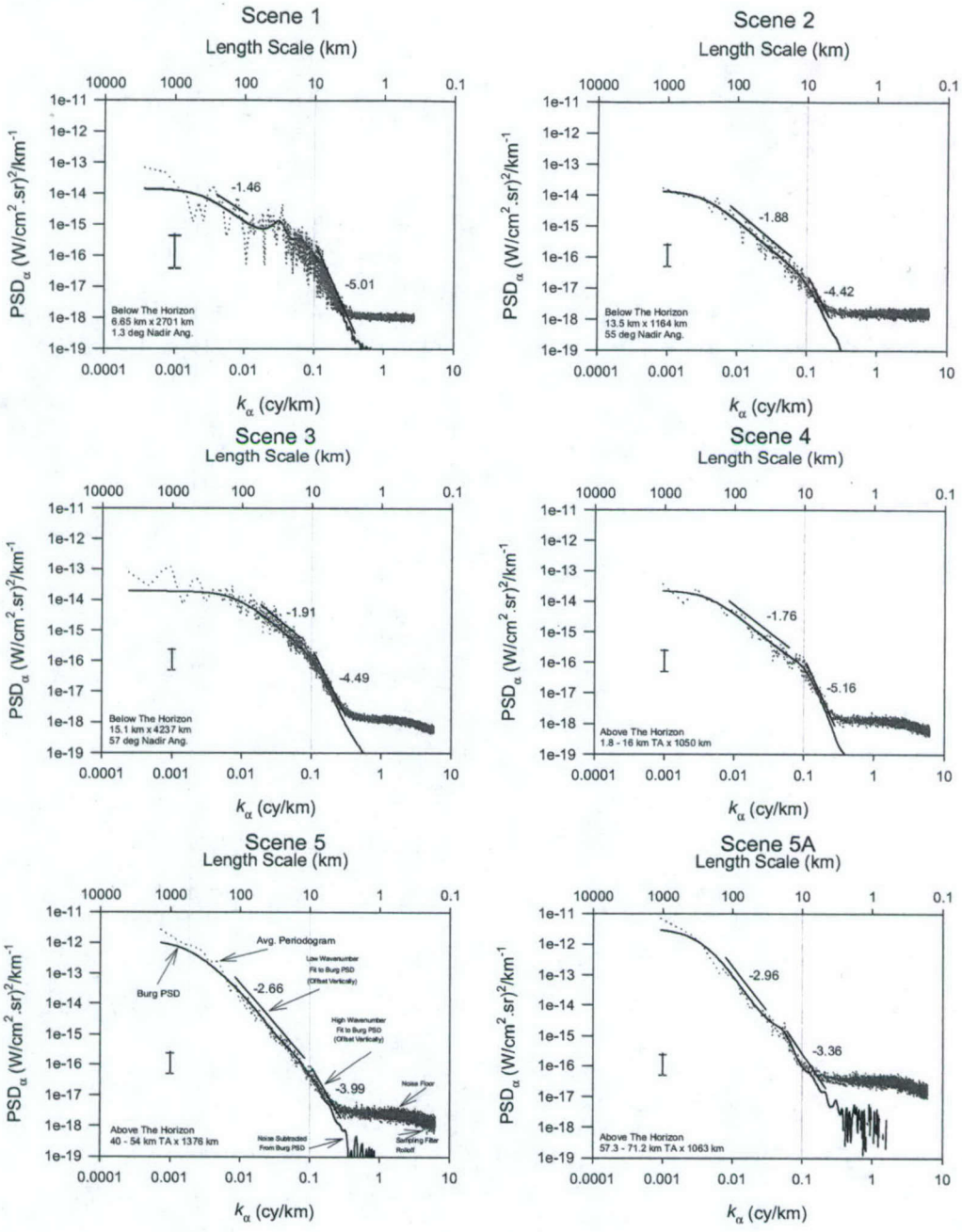

Figure 6. In-scan k_α wave number spectra of radiance fluctuations for six MSX scenes. The direction of k_α is parallel to the sensor horizontal. It is computed in the direction of the LOS at fixed nadir angles. Grey points are estimates of the averaged periodograms. Solid lines depict the AR PSD estimates. The straight line portions show estimates of the spectral slopes in the lower and higher wave number regions. The vertical bars depict estimates of the standard error of the averaged periodogram. The instrumental noise level has been subtracted from the AR PSDs, but to allow inspection, has been retained in the averaged periodograms. The numbers in the lower left portion of each plot refer to the image footprint (cross-scan by in-scan distances), TA = tangent altitude.

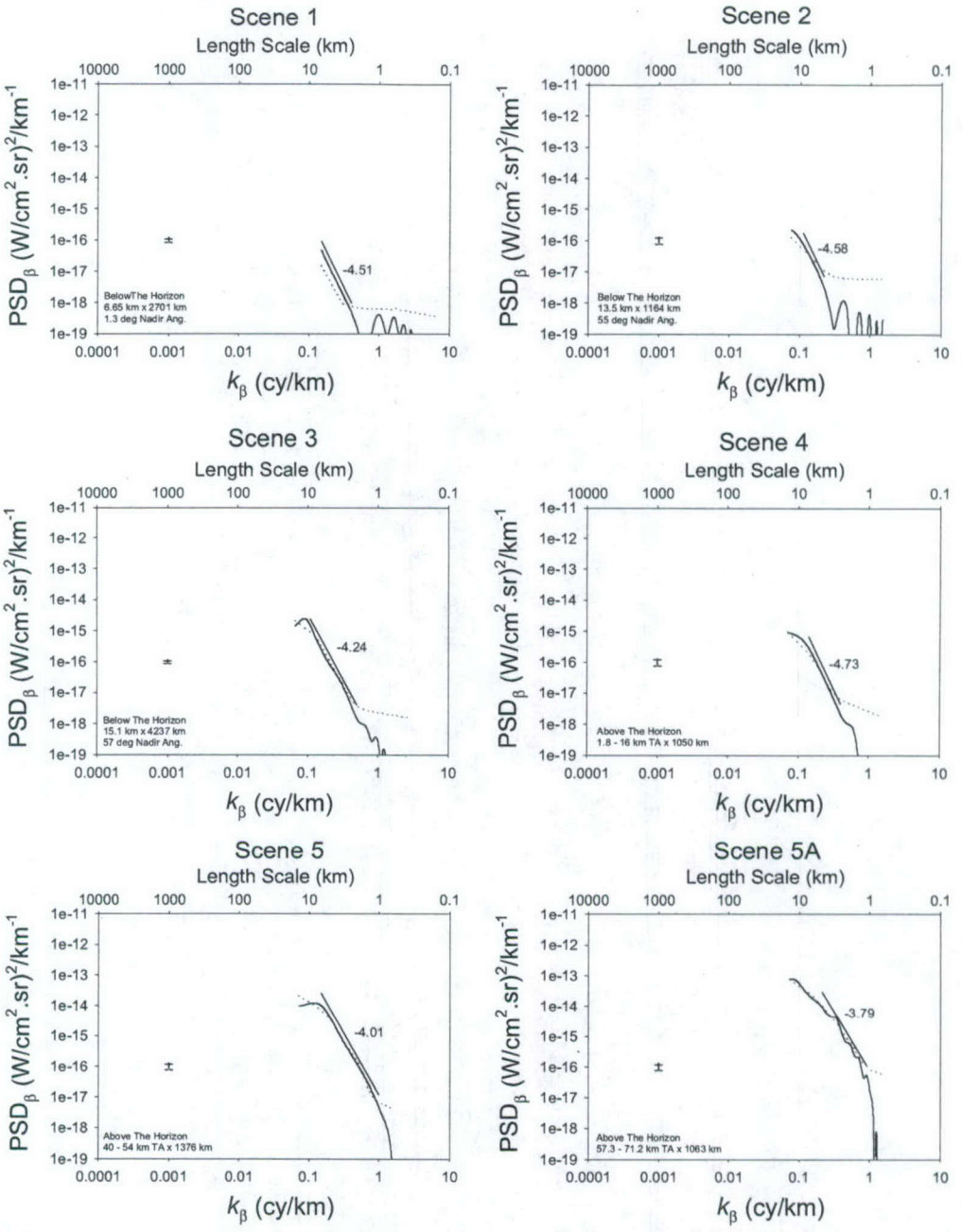

Figure 7. Cross-scan k_β wave number spectra of radiance fluctuations for six MSX scenes. The direction of k_β is parallel to the sensor vertical and is obtained orthogonal to the LOS. Grey points are estimates of the averaged periodograms. Solid lines depict the AR PSD estimates. The straight line portions show estimates of the spectral slopes. The vertical bars depict estimates of the standard error of the averaged periodogram. The instrumental noise level has been subtracted from the AR PSDs, but to allow inspection, has been retained in the averaged periodograms.

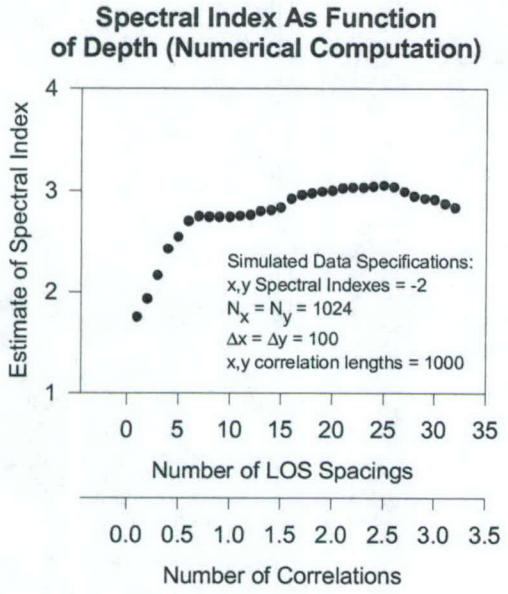

Figure 8. Numerical computation showing the transition from a k^{-n} to a $k^{-(n+1)}$ spectral index as the number of correlations along the LOS increases in an isotropic, non-separable model, fluctuation field.

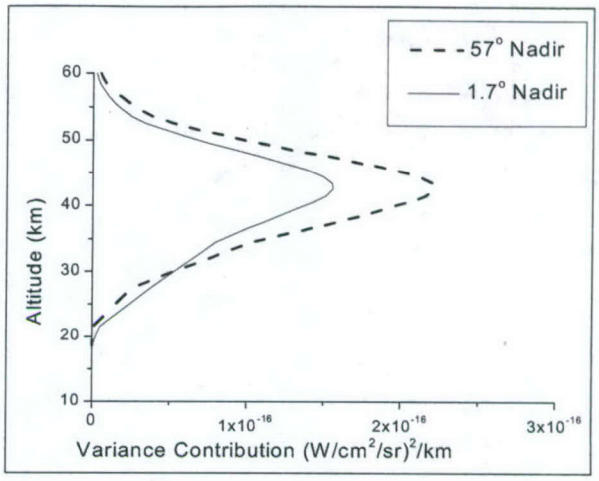

Figure 9. Model calculations of the radiance variance contribution function ($W(r,0)dr/dz$) vs. tangent altitude for the B_1 band.

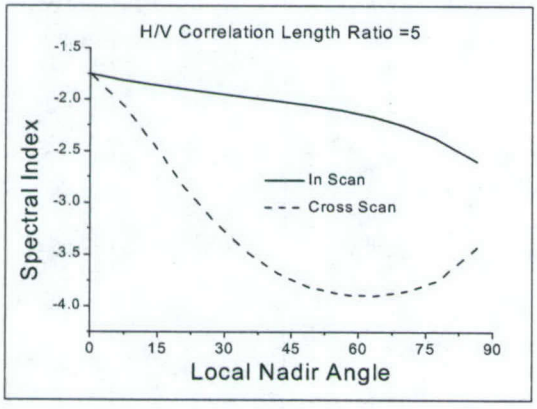

Figure 10. Model radiance spectral index as a function of local zenith angle with horizontal to vertical correlation length ratio = 5.

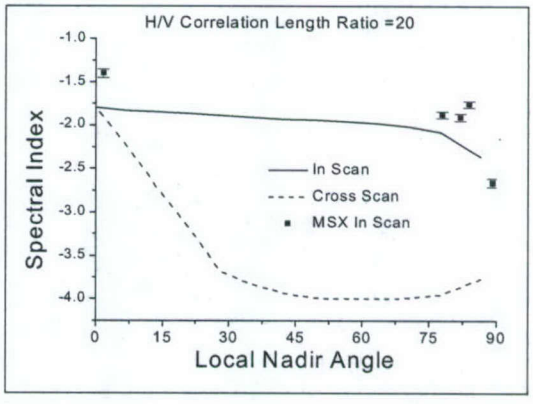

Figure 11. Model radiance spectral index as a function of local zenith angle with horizontal to vertical correlation length ratio = 20. Included on the plot are solid square symbols that show the measured MSX in-scan radiance spectral slopes from Scenes 1 to 5.